OPEN ACCESS



X-Ray Polarization Detection of Cassiopeia A with IXPE

```
Jacco Vink<sup>1</sup>, Dmitry Prokhorov<sup>1</sup>, Riccardo Ferrazzoli<sup>2</sup>, Patrick Slane<sup>3</sup>, Ping Zhou<sup>4</sup>, Kazunori Asakura<sup>5</sup>, Luca Baldini<sup>6,7</sup>
                    Niccoló Bucciantini<sup>8,9,10</sup>, Enrico Costa<sup>2</sup>, Alessandro Di Marco<sup>2</sup>, Jeremy Heyl<sup>11</sup>, Frédéric Marin<sup>12</sup>,
           Tsunefumi Mizuno 13 , C.-Y. Ng 14, Melissa Pesce-Rollins 6, Brian D. Ramsey 15, John Rankin 2, Ajay Ratheesh 2,
    Carmelo Sgró<sup>6</sup>, Paolo Soffitta<sup>2</sup>, Douglas A. Swartz<sup>15</sup>, Toru Tamagawa<sup>16</sup>, Martin C. Weisskopf<sup>15</sup>, Yi-Jung Yang<sup>14,17</sup>, Ronaldo Bellazzini<sup>6</sup>, Raffaella Bonino<sup>18,19</sup>, Elisabetta Cavazzuti<sup>20</sup>, Luigi Costamante<sup>20</sup>, Niccoló Di Lalla<sup>21</sup>,
                Luca Latronico<sup>18</sup>, Simone Maldera<sup>18</sup>, Alberto Manfreda<sup>6</sup>, Francesco Massaro<sup>18,19</sup>, Ikuyuki Mitsuishi<sup>22</sup>
        Nicola Omodei<sup>21</sup>, Chiara Oppedisano<sup>18</sup>, Silvia Zane<sup>23</sup>, Ivan Agudo<sup>24</sup>, Lucio A. Antonelli<sup>25,26</sup>, Matteo Bachetti<sup>27</sup>, Matteo Bachetti<sup>27</sup>
       Wayne H. Baumgartner<sup>15</sup>, Stefano Bianchi<sup>28</sup>, Stephen D. Bongiorno<sup>15</sup>, Alessandro Brez<sup>6</sup>, Fiamma Capitanio<sup>2</sup>, Simone Castellano<sup>6</sup>, Stefano Ciprini<sup>26,29</sup>, Alessandra De Rosa<sup>2</sup>, Ettore Del Monte<sup>2</sup>, Laura Di Gesu<sup>20</sup>, Immacolata Donnarumma<sup>20</sup>, Victor Doroshenko<sup>30,31</sup>, Michal Dovčiak<sup>32</sup>, Steven R. Ehlert<sup>15</sup>, Teruaki Enoto<sup>16</sup>, Yuri Evangelista<sup>2</sup>, Sergio Fabiani<sup>2</sup>, Javier A. Garcia<sup>33</sup>, Shuichi Gunji<sup>34</sup>, Kiyoshi Hayashida<sup>35</sup>, Wataru Iwakiri<sup>36</sup>, Svetlana G. Jorstad<sup>37,38</sup>, Vladimir Karas<sup>32</sup>, Takao Kitaguchi<sup>16</sup>, Jeffery J. Kolodziejczak<sup>15</sup>, Henric Krawczynski<sup>39</sup>, Fabio La Monaca<sup>2</sup>, Ioannis Liodakis<sup>40</sup>, Andrea Marinucci<sup>20</sup>, Alan P. Marscher<sup>37</sup>, Herman L. Marshall<sup>41</sup>, Paiscondre Benitta<sup>25</sup>, Fabio Matt<sup>28</sup>, 
 Giorgio Matt<sup>28</sup>, Fabio Muleri<sup>2</sup>, Stephen L. O'Dell<sup>15</sup>, Alessandro Papitto<sup>25</sup>, George G. Pavlov<sup>42</sup>, Abel L. Peirson<sup>21</sup>, Matteo Perri<sup>25,26</sup>, Maura Pilia<sup>27</sup>, Andrea Possenti<sup>27</sup>, Juri Poutanen<sup>31,43</sup>, Simonetta Puccetti<sup>26</sup>, Roger W. Romani<sup>21</sup>,
    Gloria Spandre<sup>6</sup>, Fabrizio Tavecchio<sup>44</sup>, Roberto Taverna<sup>45</sup>, Yuzuru Tawara<sup>22</sup>, Allyn F. Tennant<sup>15</sup>, Nicolas E. Thomas<sup>15</sup>, Francesco Tombesi<sup>29,46,47</sup>, Alessio Trois<sup>27</sup>, Sergey Tsygankov<sup>31,43</sup>, Roberto Turolla<sup>23,45</sup>, Kinwah Wu<sup>23</sup>, and Fei Xie<sup>48</sup>
     Anton Pannekoek Institute for Astronomy & GRAPPA, University of Amsterdam, Science Park 904, 1098 XH Amsterdam, The Netherlands; j.vink@uva.nl
                                             INAF Istituto di Astrofisica e Planetologia Spaziali, Via del Fosso del Cavaliere 100, I-00133 Roma, Italy
                                                    Center for Astrophysics, Harvard & Smithsonian, 60 Garden Street, Cambridge, MA 02138, USA
                                          <sup>4</sup> School of Astronomy and Space Science, Nanjing University, Nanjing 210023, People's Republic of China
<sup>5</sup> Osaka University, Graduate School of Science, Osaka, Japan
                                                   <sup>6</sup> Istituto Nazionale di Fisica Nucleare, Sezione di Pisa, Largo B. Pontecorvo 3, I-56127 Pisa, Italy
                                                               Dipartimento di Fisica, Università di Pisa, Largo B. Pontecorvo 3, 56127 Pisa, Italy
                                                           BINAF Osservatorio Astrofisico di Arcetri, Largo Enrico Fermi 5, I-50125 Firenze, Italy
                          <sup>9</sup> Dipartimento di Fisica e Astronomia, Università degli Studi di Firenze, Via Sansone 1, I-50019 Sesto Fiorentino, Firenze, Italy
                                         Istituto Nazionale di Fisica Nucleare, Sezione di Firenze, Via Sansone 1, I-50019 Sesto Fiorentino, Firenze, Italy
                                                                              University of British Columbia, Vancouver, BC V6T 1Z4, Canada
                                  <sup>12</sup> Université de Strasbourg, CNRS, Observatoire Astronomique de Strasbourg, UMR 7550, F-67000 Strasbourg, France
                     Hiroshima Astrophysical Science Center, Hiroshima University, 1-3-1 Kagamiyama, Higashi-Hiroshima, Hiroshima 739-8526, Japan
                                                                     Department of Physics, The University of Hong Kong, Pokfulam, Hong Kong
                                                                            <sup>15</sup> NASA Marshall Space Flight Center, Huntsville, AL 35812, USA
                                                         <sup>16</sup> RIKEN Cluster for Pioneering Research, 2-1 Hirosawa, Wako, Saitama 351-0198, Japan
                                                                    <sup>17</sup> Laboratory for Space Research, The University of Hong Kong, Hong Kong
                                                 <sup>18</sup> Istituto Nazionale di Fisica Nucleare, Sezione di Torino, Via Pietro Giuria 1, I-10125 Torino, Italy
                                                 <sup>19</sup> Dipartimento di Fisica, Università degli Studi di Torino, Via Pietro Giuria 1, I-10125 Torino, Italy
                                                                       ASI -Agenzia Spaziale Italiana, Via del Politecnico snc, I-00133 Roma, Italy
                <sup>21</sup> Department of Physics and Kavli Institute for Particle Astrophysics and Cosmology, Stanford University, Stanford, California 94305, USA
     <sup>22</sup> Graduate School of Science, Division of Particle and Astrophysical Science, Nagoya University, Furo-cho, Chikusa-ku, Nagoya, Aichi 464-8602, Japan
                                      Mullard Space Science Laboratory, University College London, Holmbury St Mary, Dorking, Surrey RH5 6NT, UK
                                             Instituto de Astrofísicade Andalucía, IAA-CSIC, Glorieta de la Astronomía s/n, SE-18008 Granada, Spain
                                                  INAF Osservatorio Astronomico di Roma, Via Frascati 33, I-00078 Monte Porzio Catone, Roma, Italy
                                                <sup>26</sup> Space Science Data Center, Agenzia Spaziale Italiana, Via del Politecnico snc, I-00133 Roma, Italy
                               27 INAF Osservatorio Astronomico di Cagliari, Via della Scienza 5, I-09047 Selargius, Cagliari, Italy
Dipartimento di Matematica e Fisica, Università degli Studi Roma Tre, Via della Vasca Navale 84, I-00146 Roma, Italy
                            <sup>29</sup> Istituto Nazionale di Fisica Nucleare, Sezione di Roma "Tor Vergata", Via della Ricerca Scientifica 1, I-00133 Roma, Italy
                                                  Institut für Astronomie und Astrophysik, Universität Tübingen, Sand 1, D-72076 Tübingen, Germany
                                   <sup>31</sup> Space Research Institute of the Russian Academy of Sciences, Profsoyuznaya Str. 84/32, Moscow 117997, Russia
                                             Astronomical Institute of the Czech Academy of Sciences, Boční II 1401/1, 14100 Praha 4, Czech Republic
                                                                                  California Institute of Technology, Pasadena, CA 91125, USA
                                                                Yamagata University, 1-4-12 Kojirakawa-machi, Yamagata-shi 990-8560, Japan
                                                                                Osaka University, 1-1 Yamadaoka, Suita, Osaka 565-0871, Japan
                      <sup>36</sup> Department of Physics, Faculty of Science and Engineering, Chuo University, 1-13-27 Kasuga, Bunkyo-ku, Tokyo 112-8551, Japan
                                          Institute for Astrophysical Research, Boston University, 725 Commonwealth Avenue, Boston, MA 02215, USA
                         <sup>38</sup> Department of Astrophysics, St. Petersburg State University, Universitetsky pr. 28, Petrodvoretz, 198504 St. Petersburg, Russia
                     <sup>39</sup> Physics Department and McDonnell Center for the Space Sciences, Washington University in St. Louis, St. Louis, MO 63130, USA
                                                                    <sup>0</sup> Finnish Centre for Astronomy with ESO, 20014 University of Turku, Finland
   <sup>41</sup> MIT Kavli Institute for Astrophysics and Space Research, Massachusetts Institute of Technology, 77 Massachusetts Avenue, Cambridge, MA 02139, USA
                                           Department of Astronomy and Astrophysics, Pennsylvania State University, University Park, PA 16802, USA
                                                                       Department of Physics and Astronomy, 20014 University of Turku, Finland
                                                       <sup>44</sup> INAF Osservatorio Astronomico di Brera, Via E. Bianchi 46, I-23807 Merate, Lecco, Italy
                                        <sup>45</sup> Dipartimento di Fisica e Astronomia, Università degli Studi di Padova, Via Marzolo 8, I-35131 Padova, Italy
                             <sup>46</sup> Dipartimento d<u>i</u> Fisica, Università degli Studi di Roma "Tor Vergata", Via della Ricerca Scientifica 1, I-00133 Roma, Italy
                                                            Department of Astronomy, University of Maryland, College Park, Maryland 20742, USA
```

⁴⁸ Guangxi Key Laboratory for Relativistic Astrophysics, School of Physical Science and Technology, Guangxi University, Nanning 530004, People's Republic of China

Received 2022 June 14; revised 2022 August 15; accepted 2022 August 16; published 2022 October 12

Abstract

We report on a $\sim 5\sigma$ detection of polarized 3–6 keV X-ray emission from the supernova remnant Cassiopeia A (Cas A) with the Imaging X-ray Polarimetry Explorer (IXPE). The overall polarization degree of $1.8\% \pm 0.3\%$ is detected by summing over a large region, assuming circular symmetry for the polarization vectors. The measurements imply an average polarization degree for the synchrotron component of $\sim 2.5\%$, and close to 5% for the X-ray synchrotron-dominated forward shock region. These numbers are based on an assessment of the thermal and nonthermal radiation contributions, for which we used a detailed spatial-spectral model based on Chandra X-ray data. A pixel-by-pixel search for polarization provides a few tentative detections from discrete regions at the $\sim 3\sigma$ confidence level. Given the number of pixels, the significance is insufficient to claim a detection for individual pixels, but implies considerable turbulence on scales smaller than the angular resolution. Cas A's X-ray continuum emission is dominated by synchrotron radiation from regions within $\lesssim 10^{17}$ cm of the forward and reverse shocks. We find that (i) the measured polarization angle corresponds to a radially oriented magnetic field, similar to what has been inferred from radio observations; (ii) the X-ray polarization degree is lower than in the radio band (~5%). Since shock compression should impose a tangential magnetic-field structure, the IXPE results imply that magnetic fields are reoriented within $\sim 10^{17}$ cm of the shock. If the magnetic-field alignment is due to locally enhanced acceleration near quasi-parallel shocks, the preferred X-ray polarization angle suggests a size of 3×10^{16} cm for cells with radial magnetic fields.

Unified Astronomy Thesaurus concepts: Supernova remnants (1667); Polarimetry (1278); X-ray astronomy (1810); Shocks (2086)

1. Introduction

Supernova remnants (SNRs) have long been known to be sources of radio synchrotron radiation (Shklovsky 1954), emitted by relativistic electrons, which are now recognized to be accelerated through the diffusive shock acceleration (DSA) process (e.g., Malkov & Drury 2001). According to DSA theory, energetic, charged particles move diffusively through the plasma—due to scattering on magnetic-field fluctuations and gain energy by repeatedly crossing the shock front, with each shock crossing providing a few percent gain in momentum. The presence of relativistic electrons has been key for identifying SNR shocks—as opposed to the supernova explosions themselves— as locations for Galactic cosmic-ray acceleration. Although the link between cosmic rays and SNRs has also been confirmed by gamma-ray detections of many SNRs (e.g., Helder et al. 2012; Funk 2017, for reviews), important information about the cosmic-ray acceleration process and shock conditions has been obtained from the detection and characterization of X-ray synchrotron emission from young SNRs, starting with the discovery of X-ray synchrotron radiation from the rims of SN 1006 (Koyama et al. 1995).

The ~ 10 –100 TeV electrons responsible for the X-ray synchrotron radiation have radiative-loss timescales that are short compared to the SNR ages: $\tau_{\rm loss} \approx 12.5 E_{14}^{-1} B_{-4}^{-2}$ yr, with E_{14} the electron energy in units of 100 TeV and $B_{-4} \equiv B/10^{-4}$ G. X-ray synchrotron radiation from SNRs, therefore, indicates that the 10–100 TeV electrons have been accelerated recently and on short timescales. According to DSA theory, reaching such high energies requires highly turbulent fields— $|\delta B/B| \sim 1$ —resulting in mean-free-path lengths of the order of the gyroradius for these electrons.

Original content from this work may be used under the terms of the Creative Commons Attribution 4.0 licence. Any further distribution of this work must maintain attribution to the author(s) and the title of the work, journal citation and DOI.

Synchrotron radiation is intrinsically polarized at the \sim 70% level (Ginzburg & Syrovatskii 1965), with the polarization angle informing us about the local magnetic-field orientation, and the polarization degree being dependent on the uniformity of the magnetic-field orientation along the line of sight of observed regions. Mature SNRs (\$\ge 2000 \text{ yr}) tend to have magnetic fields that are tangentially oriented with respect to the radial direction, whereas young SNRs have radially oriented magnetic fields (Dickel & Milne 1976). See also the review by Dubner & Giacani (2015). The polarization degree in the radio band is also different between young and mature SNRs, with mature SNRs generally having polarization degrees above 10%, while young SNRs (≲2000 yr) generally have polarization degrees below 10% (Dickel & Jones 1990; Sun et al. 2011). The radial orientation of the magnetic fields in young SNRs is not well understood from a theoretical point of view, but see Zirakashvili & Ptuskin (2008), Inoue et al. (2013), and West et al. (2017) for a number of hypotheses. It is not known whether the radially oriented field is immediately established at the shock front. It may well be that the fields closer to the shock fronts are tangentially oriented (Jun & Norman 1996; Bykov et al. 2020), since the shock compresses, and thus enhances, the tangential component of the preshock magnetic field.

An object that has in many ways been central to the discussion of radio and X-ray synchrotron radiation from SNRs is the young (\sim 350 yr) and bright core-collapse SNR Cassiopeia A (Cas A), located at a distance of 3.4 kpc (Reed et al. 1995). Cas A has a radially oriented magnetic field (e.g., Rosenberg 1970; Braun et al. 1987), and a polarization degree in the radio band of only 5% in the bright shell, and 8%–10% in the outer regions (e.g., Anderson et al. 1995). The \sim 5% level of polarization degree has been established at radio frequencies from 20 to 100 GHz (Mayer & Hollinger 1968; Flett & Henderson 1979; Kenney & Dent 1985) and even in the infrared, at 2.2 μ m, for a segment in the northwest of Cas A (Jones et al. 2003). At these high frequencies Faraday rotation is negligible—see also Kenney & Dent (1985)—and the only

factor contributing to the low polarization degree is the nonuniformity of the magnetic-field directions within a angular resolution element and integrated along the line of sight.

X-ray polarization measurements are in that respect highly interesting. First of all, the rapid radiative losses of the 10-100 TeV electrons mean that X-ray synchrotron emission originates from plasma that is confined to thin regions downstream of the shock, with a typical width of $l_{\rm loss} \approx \Delta v \tau_{\rm loss}$, with $\Delta v = \frac{1}{4} V_{\rm sh}$. For Cas A the shock velocity is $V_{\rm sh} \approx 5000$ –6000 km s⁻¹ (e.g., Patnaude & Fesen 2009; Vink et al. 2022). Indeed, the observed widths of the X-ray synchrotron filaments of 1''-2'' ($l \approx 10^{17}$ cm) suggest that the downstream magnetic-field local, strengths $B \approx 250-550 \,\mu\text{G}$ (Vink & Laming 2003; Bamba et al. 2005; Völk et al. 2005; Ballet 2006; Helder et al. 2012). As a result, X-ray synchrotron emission originates from a much smaller volume than the radio synchrotron emission, which originates from the entire shell with lines of sight of $l \gtrsim 10^{18}$ cm. The shorter path lengths probed in X-ray synchrotron radiation should result in less depolarization caused by variations in magnetic-field orientations along the line of sight. In addition, due to the steepness of the X-ray synchrotron spectrum, the intrinsic, maximum polarization degree could be larger than in the radio (Ginzburg & Syrovatskii 1965; Bykov et al. 2009).

However, as already stated above, the electron energies of 10-100 TeV necessary for X-ray synchrotron radiation require DSA in the presence of very turbulent magnetic fields immediately upstream of the shock fronts. Although shock compression enhances the tangential components of the magnetic field, a high level of magnetic-field turbulence may persist in the downstream region, perhaps even isotropizing the magnetic field due to nonlinear interactions of the fluctuations downstream of the shock (Bykov et al. 2020). But it is also possible that the turbulence rapidly decays within the region producing the X-ray synchrotron radiation (Pohl et al. 2005). Whatever the mechanism that created the large scale radially oriented magnetic field inferred from radio emission is, this mechanism may already start to realign magnetic fields in a radial direction immediately downstream of the shocks (Jun & Norman 1996; Inoue et al. 2013). Note that an interesting feature of the X-ray synchrotron emission from Cas A is that it does not only arise from the forward shock, but also from the reverse shock region, in particular in the western part of the SNR (Helder & Vink 2008: Uchiyama & Aharonian 2008; Grefenstette et al. 2015), where the reverse shock appears to be moving toward the center instead of outward (Sato et al. 2018; Vink et al. 2022).

With the recent launch of the Imaging X-ray Polarimetry Explorer (IXPE; Weisskopf et al. 2022), we can finally measure and map polarization with spatial resolution of a few tens of arcseconds. Cas A was the first science target of IXPE, and we report here the first detection of X-ray polarization from a shell-type SNR, albeit with a surprisingly low polarization degree of \lesssim 4%. Although IXPE cannot resolve the X-ray synchrotron filaments, the fact that X-ray synchrotron radiation originates from within \sim 10¹⁷ cm downstream of the shock (i.e., in the radial direction), allows us to probe the magnetic-field orientation and isotropy to within this distance of the shocks.

In Section 2, we describe the measurements and analysis approach and the resulting polarization measurements. In Section 3, we discuss the implications of our results in the context of models for producing polarized emission from energetic particles in SNRs. Our conclusions are presented in

Section 4. Details on the definition and treatment of the Stokes parameters, and on treatment of the unpolarized thermal emission in Cas A are given in the Appendices.

2. Observations, Data Analysis, and Results

IXPE is a NASA/ASI⁴⁹ small explorer mission that was launched on 2021 December 9. The polarization sensitive X-ray detectors are gas-pixel detectors (GPDs) filled with dimethyl ether (Costa et al. 2001; Baldini et al. 2021), which are placed at the focus of three Wolter-1 mirror module assemblies giving telescopes with angular resolutions of 24", 29", and 30" (half-power diameters) and each with a field of view of 12.9 square (see Soffitta et al. 2021; Weisskopf et al. 2022). An X-ray photon interacting with the gas in the GPD results in the ejection of a photoelectron in the direction ϕ , which is distributed as $\cos^2 \theta$, where θ is the polarization direction of the electromagnetic wave. The photoelectron ionizes the gas and produces secondary electrons, which form a charge cloud. These electrons, after drifting and multiplication, are then detected and recorded by a finely pixelated detector plane. A moments analysis of the charge-cloud shape is used to reconstruct the initial photoelectron's direction, ϕ (see Bellazzini et al. 2003, for details).

The IXPE detectors are sensitive for polarization in the X-ray range from 2 to 8 keV, with a mirror effective area of 590 cm² at 4.5 keV for the three telescopes combined, reduced to a combined 26 cm² after accounting for detector quantum efficiency. The polarization sensitivity improves with energy, having a modulation factor of $\mu \sim 15\%$ at 2 keV to $\mu = 50\%$ –60% at 8 keV. The modulation factor is the amplitude of the modulation due to polarization for a 100% polarized source in the absence of background. An ideal polarization detector will have $\mu = 100\%$. The detection of polarization also depends on the number of detected photons, which in turn depends on the source spectrum, the detector efficiency, and the telescope effective area; for IXPE, the optimum energy for detecting polarization is roughly \sim 3 keV. Cas A's 2–8 keV spectrum is dominated by K-shell line emission from Si, S, Ar, Ca, and Fe, and continuum emission that is in many regions dominated by synchrotron radiation (e.g., Helder & Vink 2008; see also Appendix B). The 4-6 keV band has only weak line emission, but while using IXPE simulations based on imaging spectroscopy with the Chandra X-ray Observatory (Chandra for short; Appendix B), we found that a priori the 3-6 keV band offered a better sensitivity for detecting polarization, despite the presence of Ar-K and Ca-K line emission.

Cas A was the first science target of IXPE, after first observing the calibration source SMC X-1 during the 1 month commissioning phase. IXPE observed Cas A from 2022 January 11 to January 29 for a total time around 900 ks. We analyzed the data with the software package <code>ixpeobssim</code> (Baldini et al. 2022), which is used both for extraction of Stokes maps and spectra, as well as for Monte Carlo simulations. The analysis was based on processed high-level event list (level two) in FITS format (see Rankin et al. 2022), which, apart from the usual columns for time, energy channel, and sky and detector coordinates, also contains columns with $q_k \equiv 2\cos 2\phi_k$ and $u_k \equiv 2\sin 2\phi_k$, with ϕ_k the reconstructed photoelectron direction of event number k. This definition is different from Kislat et al. (2015) as the factor 2 is here part of the definition of q_k and u_k . Note that the values for q_k and u_k

⁴⁹ Agenzia Spaziale Italiana.

also contain a small correction, based on the method outlined by Rankin et al. (2022), which is necessary to remove the effects of a small modulation measured for an unpolarized source, as found and calibrated on ground. The stability of these corrections have been assessed on ground. For in-flight data the stability of these corrections has not yet been assessed, but in the 3 to 6 keV band these effects are minor. We can therefore state that the results of our analysis are not affected by spurious modulation effects. For the present analysis, the values of q_k and u_k are based on the moment analysis of the charge clouds. In a future data release the determination of ϕ_k may be improved, once machine-learning algorithms, currently under development (Peirson & Romani 2021), are employed.

During the early observations a number of calibration issues emerged and several corrections were applied. First of all, we filtered out likely particle background events using the electron tracks, as described by Xie et al. (2021) (see also A. Di Marco et al. in preparation). The fraction of the particle background removed was $\sim 30\%$, while less than 1% of the source was rejected. We found, however, the impact of the particle background on the polarization signal of Cas A to be negligible. Second, the reconstructed energies of the IXPE detected events in the level-two data are known to have detector-dependent and time-dependent deviations, due to various effects, including charge built up in the detectors. Throughout the whole observation the three detectors were calibrated during Earth occultations, by using onboard calibration sources, producing line emission at 1.7 keV (Si K α) and 5.9 keV (55 Fe decaying into ⁵⁵Mn; Ferrazzoli et al. 2020). Given the linearity of the response, the two energies allow for measuring both the slope and bias of the calibration. We reconstructed the time dependency of the channel-to-energy conversion. Third, the boom connecting the X-ray telescopes with the spacecraft was affected by phasedependent heating during its orbit around Earth. As a result the boom experienced time modulated bending, resulting in the focal point changing in detector coordinates. Corrections to these phase-dependent effects, some of which were also applied to the publicly released level-two event list, still left an overall pointing reconstruction offset of the order of 2.15. In order to remove the offset we employed a spatial correlation code developed for measuring the expansion of Cas A (Vink et al. 2022), and used it to register the pointing solution of each detector unit to the 2019 (Observation ID (ObsID) 19606) observation of Cas A with Chandra, for which we smoothed the Chandra image with $\sigma = 10$."4. For this we used the 4–6 keV continuum band, as the morphology of Cas A in this band is relatively independent of the energy response of the detectors. This resulted in a pointing solution with an accuracy of about 1"-2". Finally, during the orbit, the pointing is affected by a switch between the two different star trackers, one placed near the mirror module assemblies and viewing forward, and one placed on the spacecraft and looking in opposite direction. Currently this results in small periods of time with offsets in the pointing solutions. For the present analysis we filtered these short intervals out, leaving 819 ks of effective exposure time.

2.1. Spatial Exploration of Polarization Signals

Maps of the Stokes parameters I, Q, and U are made with sums of u_k and q_k and a correction to account for the energy-dependent modulation factor. See Appendix A for details. All maps shown are based on the summed maps of the three detector units. For the present analysis we did not use weights

as we found that weighting with the modulation factor $w_k \propto \mu_k^{-2}$ (Vink & Zhou 2018) resulted only in minor to no improvements in the statistical significance.

In Figure 1 we show the Stokes I three-band color map of Cas A with a pixel size of 10"4, and the 3–6 keV map of the minimal detectable polarization at 99% confidence level (MDP99, see Appendix A) for a pixel size of 42". The MDP99 map shows that polarization on these pixel scales can be detected at the \sim 5% polarization degree level in the interior regions, and up to 15% in the fainter outer regions. All maps also show the 4–6 keV contour lines based on Chandra observations, which serve as a point of reference for all derived polarization maps. Figure 1 includes a hardness ratio map based on the 4-6 keV and 3.4-3.6 keV maps as observed by Chandra. The 3.4–3.6 keV band is also relatively devoid of line emission so this hardness ratio map shows which regions emit hard, and which regions emit soft X-ray continuum (see Figure 6 in Helder & Vink 2008). The hard X-ray continuum likely corresponds to synchrotron radiation, whereas the softer continuum is dominated by thermal bremsstrahlung given that the typical electron temperatures within Cas A are $0.5 \lesssim T_e \lesssim 4.5 \text{ keV}$ (Hwang & Laming 2012, see also Appendix B). The hardness map illustrates in what regions X-ray synchrotron radiation is likely dominating the continuum emission: in the outer regions, and in some parts of the interior region—mostly the center, but with a prominent spot in the western interior region of Cas A. See also Appendix B. Although the energy resolution of IXPE is limited—with $\Delta E \approx 0.5$ keV at 2 keV and scaling inversely as the square root of the energy—one can still appreciate in the Stokes I map (Figure 1, left) that the western part and outer regions have harder spectra (showing up bluish). The spectral capabilities can also be assessed from the detector one spectrum shown in Figure 2 for three extraction regions. The Si-K and S-K line emission do not show up as broadened lines as is the case with CCD spectra, but rather lead to noticeable inflections around 3 keV (Si-K and S-K) and around 6 keV (caused by Fe-K emission). For the current paper we concentrated fully on the spatial analysis.

Analyzing the full Q and U maps we did not find any regions for which we can report a significant detection of a polarization signal. We did find regions with polarization signals above the 3σ pretrial confidence level. However, given that the statistics depend on the pixel size used, and also on the fact that Cas A is covered by about ~ 200 angular resolution regions 50 , we cannot confidently say that our analysis of the Q and U maps provide significant detections. For example, for 200 pixels the expected number of false-positive detections at the 3σ level (99.73% confidence) is 0.5 pixel. The posttrial probability for a spurious detection at the pretrial 3σ level is 42% (= $1-(99.73\%)^{200}$).

Nevertheless, the $\sim 3.5\sigma$ signals do deserve to be mentioned, first because future, improved data analysis or additional data may be able to confirm these signals as solid detections, and second because these polarization "hotspots" illustrate the low level of X-ray polarization degree of Cas A on small scales.

In Figure 3 we show two maps of polarization significance (using a χ^2_2 -map) and the polarization degree for pixel sizes of 42" and 84". For the polarization degree map we only show the pixels with detection confidence above 99.73% confidence level. The most significant signal has $\chi^2_2 = 15.9$, corresponding to a 3.57σ confidence level. The hotspots correspond to polarization degrees ranging from 3.4% (inner region, using

 $[\]overline{^{50}$ Cas A has a diameter of $\approx 5.5'$, which can be covered by ~ 174 pixels of 25''.

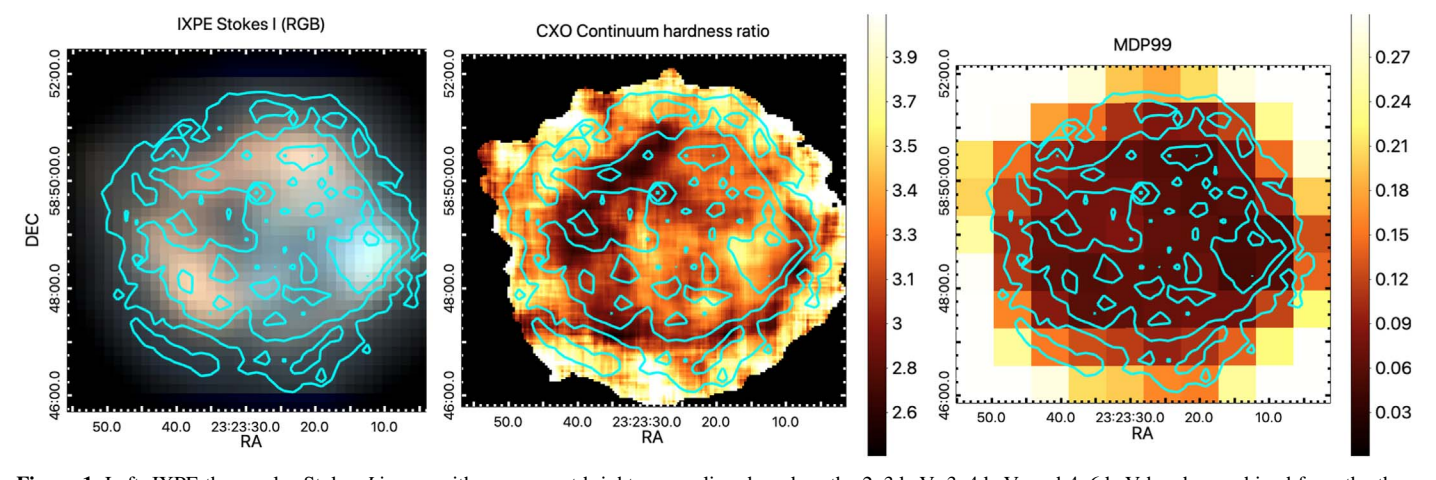


Figure 1. Left: IXPE three color Stokes I image with square-root brightness scaling, based on the 2–3 keV, 3–4 keV, and 4–6 keV bands, combined from the three detectors. The pixel size is $10.^{\prime\prime}.4$, oversampling the IXPE angular resolution by a factor \sim 2, and the images have been smoothed with a Gaussian kernel with $\sigma = 10.^{\prime\prime}.4$. Center: hardness ratio map based on Chandra X-ray data (ObsID 19606) using the 4.0–6.0 keV map divided by the 3.4–3.6 keV map, both dominated by continuum emission. The harder ratios (\gtrsim 3) likely correspond to synchrotron dominated continuum emission. Fluctuations due to differential absorption across the SNR are at the 9% level. Right: the MDP99 levels for the 3–6 keV band for the IXPE observations of Cas A. Here the map is binned to a pixel size of 42 $^{\prime\prime}$. In all panels we show the contours based on a recent 4–6 keV Chandra map using square-root brightness scaling (ObsID 19606).

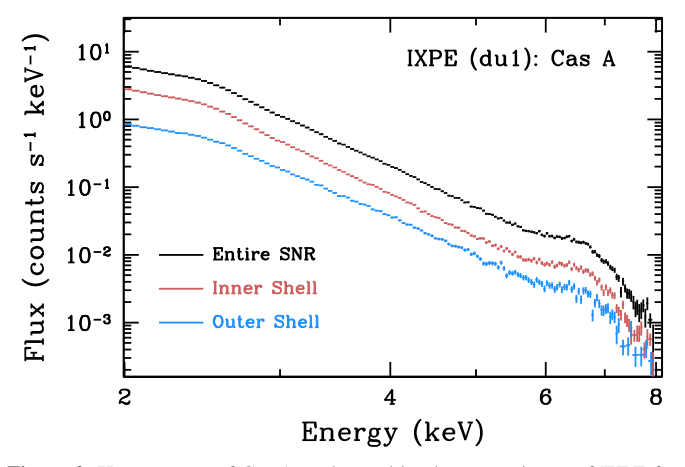


Figure 2. X-ray spectra of Cas A as detected by detector unit one of IXPE for three different extraction regions. The spectrum oversamples the spectral resolution, which is $\Delta E \approx 0.5$ at 2 keV—see Appendix B for sample spectra of Cas A at a higher spectral resolution as obtained with the Chandra ACIS-S detector.

84" pixels) to 19% (outer, forward shock region, using 42" pixels). These values are just above the MDP99 level. In the future, with an improved analysis chain, we may be able to lower the MDP99 level and increase sensitivity to regions with lower degrees of polarization.

2.2. Analysis Based on an Assumed Circular Magnetic-field Topology

The pixel-by-pixel polarization measurement yielded tentative detections of polarization with polarization degrees of 4%–15% at the 3σ – 4σ confidence level, too low to claim a solid detection. Binning into larger pixel sizes improves the polarization statistics, but at the expense of potential depolarization due to the mixing of regions with different polarization angles. However, given the roughly spherical symmetry of Cas A itself, as well as the long-known radial symmetry of the magnetic-field orientation as inferred from radio observations, one can improve the statistics by summing over large regions by assuming a circular symmetry to the polarization direction.

Although the radio polarization measurements suggest an a priori radial magnetic-field orientation, shock compression of a highly turbulent magnetic field instead would lead to an enhancement of the tangential component (e.g., Jun & Norman 1996; Bykov et al. 2020). Note that the polarization direction for synchrotron radiation is perpendicular to the magnetic-field orientation: a tangential polarization signal corresponds to a radial magnetic field, and vice versa.

Assuming a circular symmetry for the polarization direction, we recalculated the q_k and u_k values for each event, by calculating a new zero for the direction of the photoelectron (ϕ) based on the sky coordinate, and its position angle with respect to the center of Cas A, for which we used the explosion center determined by Thorstensen et al. (2001). This procedure results in new values q_k' and u_k' , which can be summed over large regions to provide an overall signal corresponding to the radial and tangential Stokes parameters Q' and Stokes U'.

In Figure 4 we show the chosen annuli for which we obtained Q' and U'. They cover the central region, the reverse shock regions (overlapping with the bright shell), and the outer region, which contains the synchrotron filaments associated with the forward shock. Since the western reverse shock region shows evidence for strong X-ray synchrotron emission (e.g., see Helder & Vink 2008; Grefenstette et al. 2015, and also the bluish part in the multiband Stokes I image in Figure 1), we also isolate just the western part of the reverse shock region.

The resulting polarization measurements are listed in Table 1. Apart from the polarization degree we list under "PD Corrected", the inferred polarization degree is of the synchrotron component only. The correction factors are based on a full modeling of the expected IXPE data by folding the Chandra best-fit spectral models through the IXPE spectral and spatial response functions using <code>ixpeobsim</code>. The Chandra best-fit spectral models and their implications for the nonthermal flux fraction are detailed in Appendix B. We stress here that the corrected PD is model-dependent as it is based on spectral fitting results. Nevertheless, the finding reported in the Appendix that up to 99% of the continuum flux is synchrotron radiation is supported by NuSTAR observations showing that an extrapolation of the hard X-ray (synchrotron) spectrum extrapolated to the 4–6 keV band accounts for a dominant

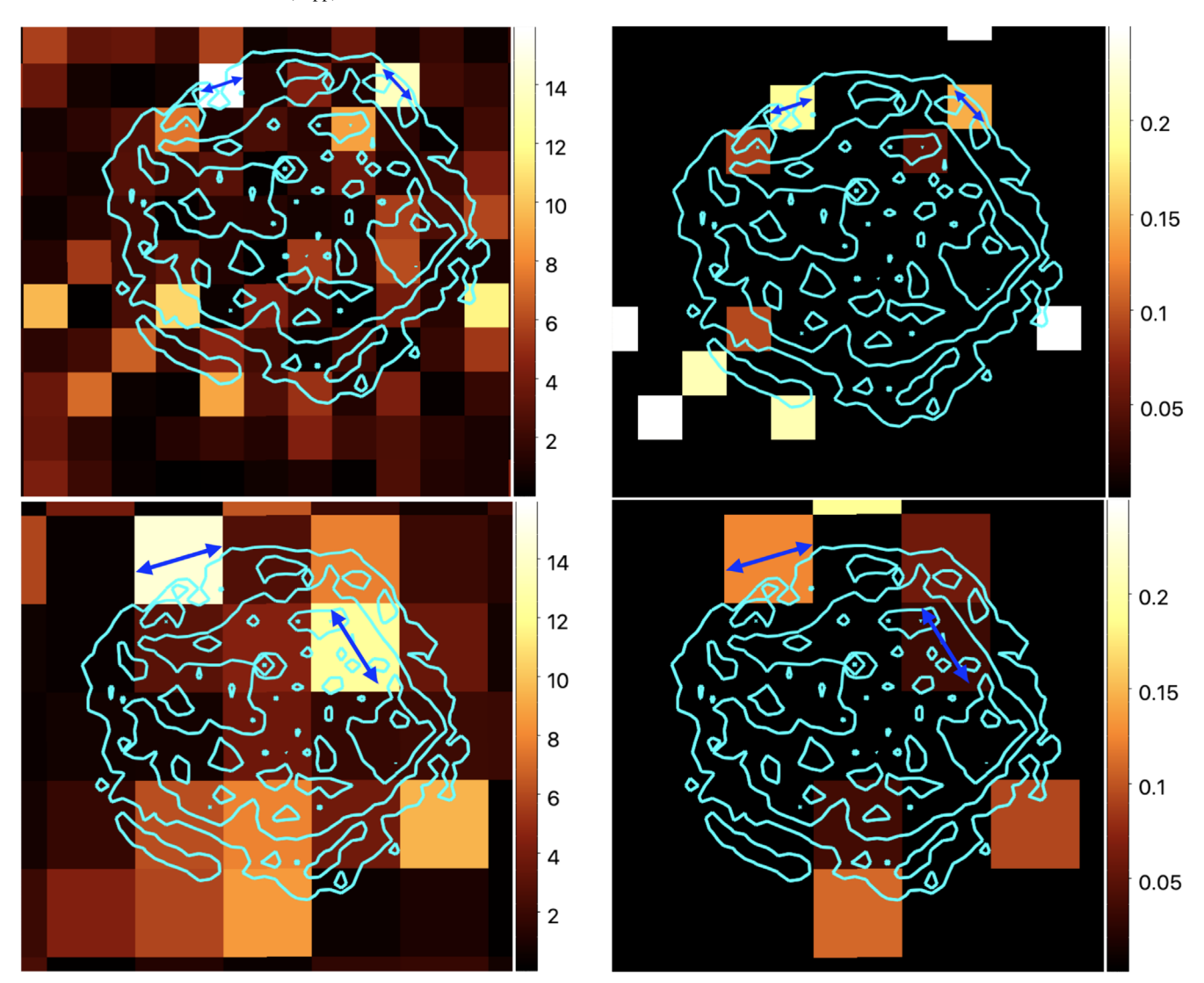


Figure 3. Left: maps of χ^2_2 (or $S_{i,j}$, see Appendix A) values for the polarization signal for the 3–6 keV band. Right: the corresponding polarization degree maps. Only pixels with pretrial confidence levels above 2σ ($\chi^2_2 > 6.28$) are shown. For pixels with $\chi^2_2 > 11.8$ (corresponding to 3σ confidence level) the polarization angles are indicated with blue arrows. The errors on these angles are \sim 8°. Top row: maps with pixel sizes binned to 42''. Peaks in the χ^2_2 map are $\chi^2_2 = 15.9$, 13.6 corresponding to polarization degrees of 19% and 14.5%. Bottom row: same plot, but with a larger pixel size of 84". Peaks in the χ^2_2 map are $\chi^2_2 = 14.4$, 12.3 corresponding to polarization degrees of 12.4% and 3.4%.

fraction of the continuum flux (see Figure 5 in Grefenstette et al. 2015).

In Appendix C we show the breakdown of the polarization signals for the "All" and "FS+RSW" regions in the 3–4 keV and 4–6 keV bands, which shows that even for the nearly lineless 4–6 keV band the measured polarization degree is indeed low, although measured at a lower significance.

The errors listed should be used with caution, since polarization degree and polarization angle are not independent statistical quantities, both being derived from a combination of Q' and U'. A better representation of the measurements is obtained by graphically representing the Stokes Q' and U' parameters in a polar diagram, with confidence contours. These are plotted in Figure 5, which shows that for the "forward shock region" and the "forward shock + western region" the 1σ confidence contour is outside the MDP99 region (in pink). For the "forward shock region" the polarization detection significance is over 4σ pretrial, corresponding to a roughly 3σ posttrial confidence level, while for the "forward shock + west region"

and all data combined the detection is close to a 5σ pretrial confidence level, corresponding to a better than 4σ posttrial confidence level. Pretrial refers here to the confidence level for polarization detection for a given region, whereas posttrial corrects for the fact that we are attempting to measure polarization for three independent regions. Note that the underlying statistics are not Gaussian, so the quoted σ values are for ease of interpretation, whereas the diagrams show the full confidence areas in the polarization-degree versus polarization-angle plane. For the most significant detections we find that the polarization angle is consistent with a tangential polarization pattern, corresponding to a radial magnetic-field orientation.

3. Discussion

The IXPE observations of Cas A reveal that the polarization level is low at the spatial resolution of IXPE ($\sim 30''$), with a tangentially oriented polarization component with a polarization degree of $\approx 1.5\%$ to $\approx 3.5\%$, corresponding to $\approx 2.5\%$ to $\approx 5\%$ for the synchrotron component only. The polarization signal is

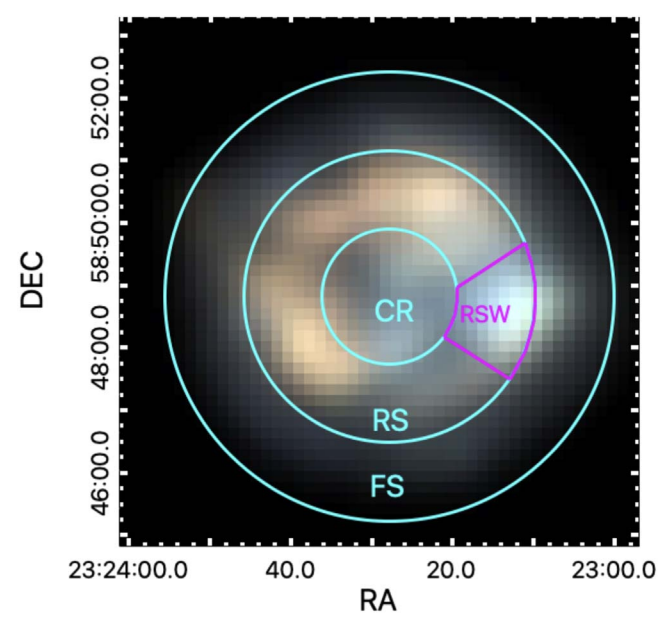


Figure 4. IXPE map, similar to Figure 1, with superimposed regions that were used to test for an overall radial or tangential polarization vector orientation. See Table 1.

associated with the X-ray synchrotron bright features in Cas A: the outside region associated with the forward shock, and the western part of the reverse shock region (see Vink & Laming 2003; Helder & Vink 2008; Uchiyama & Aharonian 2008; Grefenstette et al. 2015, for maps of the X-ray synchrotron radiation). The detection of the weak polarization signal requires the assumption of circular symmetry, but even without this assumption the polarization degree cannot be much larger than 4% for the interior (reverse shock) of Cas A, and 15% at the outer boundary, as indicated by the MDP99 levels, and the tentative indications of polarization for individual regions with angular extents of $\sim 42''-84''$. High degrees of polarization may be present for unresolved regions and they need to have more or less random polarization directions.

The low polarization degree and the tangential polarization pattern are compatible to what has been measured in the radio band (e.g., Rosenberg 1970; Braun et al. 1987; Anderson et al. 1995). Nevertheless, these X-ray polarization results still come as a surprise. First of all, in X-rays the synchrotron spectrum has steepened, leading to higher intrinsic polarization degrees (Ginzburg & Syrovatskij 1967; Bykov et al. 2009). Second, X-ray synchrotron radiation in Cas A originates from a narrow region of $\lesssim 10^{17}$ cm immediately downstream of the shocks, which reduces depolarization caused by the line-of-sight crossing regions with different polarization angles. And third, at the shock front the perpendicular (tangential) component of the magnetic field is compressed, so close to the shock front a radial instead of a tangential polarization angle is expected.

Apart from line-of-sight effects, a low polarization degree may indicate a turbulent magnetic field, in particular for angular scales smaller than the IXPE angular resolution. The level of magnetic-field turbulence near the shock regions in Cas A is expected to be high, as a high level of turbulence is required for accelerating electrons to ≥10 TeV—the energy needed for producing X-ray synchrotron radiation. However, efficient DSA assumes a high magnetic-field turbulence in the unshocked plasma, whereas the shock

compression should enhance the tangential component of the magnetic field.

The origin of the magnetic-field turbulence necessary for DSA is often attributed to the interactions of cosmic rays in the precursor with the preshock plasma. These interactions are divided into resonant and nonresonant cosmic-ray interactions (see Marcowith et al. 2016, for a review). For the resonant interactions the energetic charged particles interact and amplify Alfvén waves with wavelengths comparable to the gyroradii of the cosmic-ray particles. A prime example of a nonresonant interaction is the Bell streaming instability (Bell 2004). It is caused by the response of the plasma to the electric current driven into the plasma by the cosmic rays. Apart from cosmic-ray induced magnetic-field turbulence, which is expected to affect the preshock magnetic turbulence, the shock itself may also induce postshock turbulence. For example, recent MHD simulations by Hu et al. (2022) show substantial postshock magnetic-field turbulence, which may be contributing to the low polarization degree in the X-ray synchrotron filaments. Moreover, collisionless shocks in the heliosphere are known to be rippled, rather than smooth (see for example Gedalin & Ganushkina 2022, and references therein). If these ripples are also present for the higher Mach number collisionless shocks in Cas A, they may also affect its postshock magnetic-field turbulence.

Simulations of X-ray polarization signals to be expected for young SNRs by IXPE by Bykov et al. (2020) predicted polarization degrees of 30%–70%, assuming an anisotropic magnetic field, i.e., with a preferred orientation due to shock compression, and with a turbulence spectrum cutting off at 10^{18} cm, which is compatible with the IXPE angular resolution. For isotropic magnetic fields the polarization degree predicted by Bykov et al. (2020) is similar to the values reported here: $\sim 5\%$ –15%. Based on these models the magnetic-field turbulence near the shock may be close to isotropic, perhaps due to nonlinear interactions of the fluctuations downstream from the shock, as hypothesized by Bykov et al. (2020). In addition, it may also indicate that the magnetic-field turbulence wavelength cutoff is well below the cutoff of 10^{18} cm assumed for the simulations by Bykov et al. (2020).

Indeed, the theoretical expectations for the maximum turbulence wavelength suggest values well below 10^{18} cm. For the resonant instability one needs to consider the gyroradius of the particles, which is $r_{\rm g}=3\times10^{15}E_{14}B_{-4}^{-1}$ cm. Even if protons are accelerated up to $10^{15}\,{\rm eV}$ —for which there is no evidence for the case of Cas A (Ahnen et al. 2017)—we expect that the turbulence cuts off at length scales of $< 10^{16}\,{\rm cm}$, much smaller than the IXPE pixel size, and also smaller than the thickness of the X-ray synchrotron emitting region of $\sim 10^{17}\,{\rm cm}$.

For the longest length scales caused by the nonresonant Bell instability we refer to Equation (21) in Bell (2004). This equation predicts for $V_{\rm sh} = 5500 \, {\rm km \, s}^{-1}$ a maximum length scale for magnetic-field turbulence of $l_{\rm Bell} \approx 8 \times 10^{16} E_{\rm max,14} (B_0/3~\mu G)$ cm; B_0 refers to the preamplified parallel magnetic-field component, and $E_{\rm max,14}$ to the maximum energy of the cosmic rays in units of 10^{14} eV. This shows that even for $E_{\rm max} = 10^{15}$ eV the maximum turbulence scale for the Bell instability is less than 10^{17} cm— too small for IXPE to detect peaks in the polarization signal caused by the largest scale turbulence modes.

An alternative reason for the low degree of polarization may be that the synchrotron emission is coming from a mix of plasma with the expected tangential oriented magnetic field

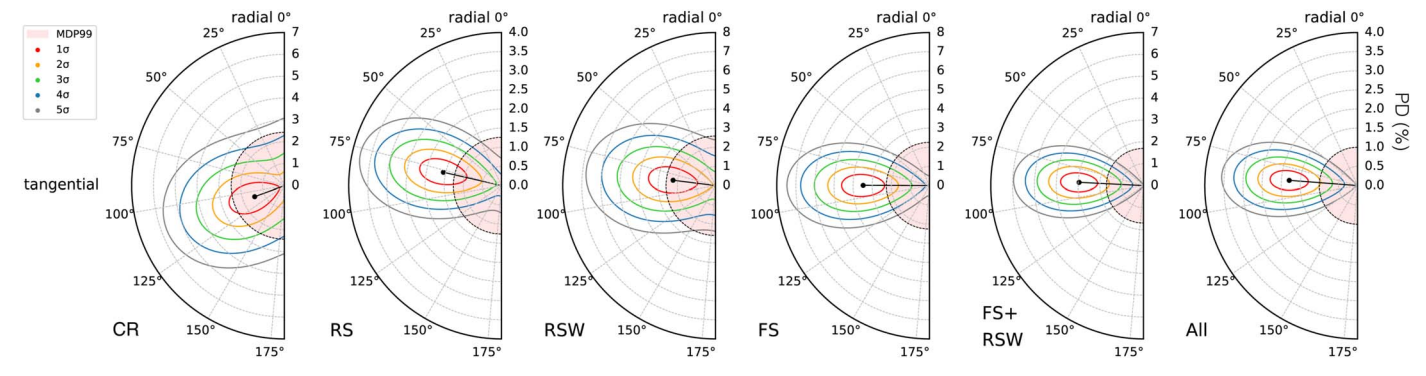


Figure 5. Polar diagrams depicting the measured polarization degree and angle with respect to circular symmetry as confidence contours for the six regions listed in Table 1. The radial coordinate indicates the polarization degree in percent. The pink region corresponds to the MDP99 level. Values around 90° correspond to an overall tangentially oriented polarization averaged over the region, while around 0° indicates on average a radially oriented polarization.

 Table 1

 Polarization Measurements in Annuli and Western Region after Imposing Circular Symmetry for Stokes U and Q^a

	R _{min} ^b (arcsec)	R _{max} (arcsec)	MDP99 (%)	Pol. Degree (%)	PD Corrected ^c (%)	Angle ^d (°)	Significance
Central region	0	65	2.4	<3.1	<3.7	N/A	0.9σ
Reverse shock (RS)	65	140	1.3	1.6 ± 0.4	2.2 ± 0.6	77.2 ± 7.6	3.1σ
RS West (RSW) ^e	65	140	2.6	< 3.9	< 5.1	N/A	1.9σ
Forward shock (FS)	140	216	2.3	3.5 ± 0.7	4.5 ± 1.0	89.8 ± 6.1	4.1σ
$FS + RSW^f$	216	216	1.7	3.0 ± 0.6	3.8 ± 0.7	87.2 ± 5.4	4.8σ
All	0	216	1.0	1.8 ± 0.3	2.5 ± 0.5	85.7 ± 5.2	4.9σ

Notes.

immediately downstream of the shock, and a more radially oriented magnetic field further downstream of the shock, but still within 10^{17} cm of the shock.

Although a radial magnetic-field orientation throughout the SNR has been inferred from radio observations, its origin has never been fully understood. There are two main hypotheses: (i) there are MHD processes stretching the magnetic fields, and (ii) the radial magnetic field is the result of a selection effect, related to efficient acceleration wherever the magnetic-field orientation at the shock happens to be quasi-parallel.

As for hypothesis (i), it was long suspected that the radially oriented magnetic fields are caused by filamentation due hydrodynamical instabilities, such as Rayleigh-Taylor instabilities at the contact discontinuity between shocked ejecta and shocked circumstellar plasma (Gull 1973). MHD simulations confirm the formation of a radially oriented magnetic field near the contact discontinuity, but the regions near the forward shock are predicted to have a tangential magnetic field (Jun & Norman 1996). Inoue et al. (2013) performed MHD simulations of the shock front in the presence of a clumpy medium, resulting in Richtmeyer-Meshkov instabilities, which reorient the overall magnetic-field orientation from a tangential to a radial direction within a distance of $\sim 7 \times 10^{17}$ cm from the shock. This length scale is almost an order of magnitude larger than the width of the X-ray synchrotron filaments, but the MHD length scale is dependent on environmental conditions, such as the size and density contrasts of the clumps. Very Large Array radio

polarization measurements by Gotthelf et al. (2001) lend some support to this hypothesis, as they report a swing in the polarization angle near the forward shock. However, the radio polarization measurements were based on an azimuthal integration over 55°, resulting in an effective spatial resolution that is larger than the widths of the X-ray filaments.

Regarding hypothesis (ii), West et al. (2017) investigated what the impact is if DSA preferentially occurs wherever the shock has a quasi-parallel magnetic-field orientation (i.e., a significant component parallel to the shock velocity vector), motivated by the likely magnetic-field orientation in SN 1006 (Rothenflug et al. 2004). As the plasma is advected downstream and keeps roughly its magnetic-field orientation, the synchrotron radiation becomes biased toward radial magnetic fields. The likely reason for efficient electron acceleration at quasi-parallel shocks probably concerns the initial injection of low energy electrons into the acceleration process. If the observational selection bias still pertains to X-ray synchrotron radiation, the implication is that the responsible \$10 TeV electrons should not have diffused too far away from the original regions with preferentially radial magnetic fields. This would imply that the shock regions with quasi-parallel magnetic fields are associated with a characteristic turbulence wavelength, λ_B , which must be comparable in size to the diffusion length scale ($l_{\rm diff}$). For $l_{\rm diff} \ll \lambda_B$ one expects a strong polarization signature, whereas for $l_{\rm diff} \gg \lambda_B$ the selection effect hypothesis by West et al. (2017) should not pertain to X-ray synchrotron radiation. The relevant diffusion length scale is that for the tangential diffusion component, which should be

^a See main text for an explanation. Listed errors correspond to 1σ (68% confidence) ranges.

b The central coordinate used was R.A. $_{J2000} = 23^{\text{h}}23^{\text{m}}27.8^{\text{s}}$, decl. $_{J2000} = 58^{\circ}48'49''.4$, which is the explosion center determined by Thorstensen et al. (2001).

^c The inferred polarization degree for the synchrotron component only; see Appendix B.

d An angle of 90° corresponds to a tangential polarization vector associated with a radial magnetic-field orientation.

e This region is a subset of the "reverse shock" region.

f This combines the reverse shock west and forward shock region.

 $l_{\rm diff} \approx \sqrt{D au_{\rm loss}} \approx 3 \times 10^{16} \eta^{1/2} (B/250~\mu G)^{-1/2}$ cm, with the diffusion coefficient given by $D = \frac{1}{3} \eta c E/(eB)$, where $\eta \geqslant 1$ is the ratio between the mean-free path of the particles and their gyroradius (see Section 1 for the other definitions). The length scale of 3×10^{16} cm corresponds to 0."6, which is comparable to the Chandra point-spread function. Since the X-ray synchrotron filaments as seen by Chandra appear to be smooth, hypothesis (ii) requires the diffusion length scale to be smaller than 3×10^{16} cm, requiring $\eta \sim 1$ and $B > 250~\mu G$.

So although the IXPE observations do not favor one hypothesis for the radial magnetic-field orientation over the other, the measured polarization signal puts constraints on relevant length scales. For the hypothesis that an MHD process leads to intrinsically radial magnetic-field alignments—rather than through a perceived radial magnetic field (West et al. 2017)—the IXPE results require that the reorientation happens within 10^{17} cm downstream of the shock. In contrast, the hypothesis that the radial magnetic-field orientation is caused by a selection effect sets constraints on the wavelength of the magnetic-field turbulence of $\lambda_B \lesssim 3 \times 10^{16}$ cm.

4. Conclusions

We reported here on the very first detection of X-ray polarization from a shell-type SNR—the young and bright core-collapse SNR Cas A, which was the first science target of the NASA IXPE mission. We employed two different methods to measure the polarization signals: a pixel-by-pixel analysis, and a more sensitive analysis that assumes a circular symmetry for the polarization vectors, and then summing over large regions.

The pixel-by-pixel analysis provides tentative hints of polarization in the 3-6 keV band at the 3σ to 4σ pretrial confidence level, with associated polarization degrees ranging from 3% to 19%, just above the local minimum detectable polarization degree at 99% confidence (MDP99). Taking into account posttrial factors these detections are not significant. The analysis assuming circular symmetry for the polarization angles provides solid detections (close to 5σ) for annular regions encompassing the forward shock region, and a region covering the entire SNR. The corresponding polarization degrees are lower than the polarization generally reported in the radio: 1.8%–3.5% in X-rays versus \sim 5% in the radio band (e.g., see Rosenberg 1970, for radio polarization measurements with a resolution comparable to IXPE). Even after correction for the contribution of thermal X-ray emission in the 3-6 keV band, this suggests an X-ray synchrotron polarization degree of \sim 2%–5%, which is similar, or slightly lower than in the radio band. Like in the radio band, the polarization vectors suggest an overall radial magnetic-field orientation.

Since the X-ray synchrotron radiation is confined to regions within $\lesssim 10^{17}$ cm, the IXPE results imply that the radial magnetic-field structure is already present close to the shock, which puts constraints on the physical processes that leads to the radial magnetic-field structures measured in young SNRs.

The measured low polarization degree is consistent with a nearly isotropic magnetic-field turbulence as simulated by Bykov et al. (2020), but it could also be caused by a mixture of tangential magnetic-field alignment close to the shock front, and a radially aligned magnetic-field structure further downstream of the shock.

The Imaging X-ray Polarimetry Explorer (IXPE) is a joint US and Italian mission. The US contribution is supported by

the National Aeronautics and Space Administration (NASA) and led and managed by its Marshall Space Flight Center (MSFC), with industry partner Ball Aerospace (contract NNM15AA18C). The Italian contribution is supported by the Italian Space Agency (Agenzia Spaziale Italiana, ASI) through contract ASI-OHBI-2017-12-I.0, agreements ASI-INAF-2017-12-H0 and ASI-INFN-2017.13-H0, and its Space Science Data Center (SSDC), and by the Istituto Nazionale di Astrofisica (INAF) and the Istituto Nazionale di Fisica Nucleare (INFN) in Italy. This research used data products provided by the IXPE Team (MSFC, SSDC, INAF, and INFN) and distributed with additional software tools by the High-Energy Astrophysics Science Archive Research Center (HEASARC), at NASA Goddard Space Flight Center (GSFC). J.V. and D.P. are supported by funding from the European Union's Horizon 2020 research and innovation program under grant agreement No. 101004131 (SHARP). The research at Boston University was supported in part by National Science Foundation grant AST-2108622. We thank Dawoon Kim for kindly providing us with his script for making polar plots of polarization degree and

Software: ixpeobsim (Baldini et al. 2022).

Appendix A Calculation of the Q and U Maps

The polarization of radiation as measured by IXPE is calculated based on the reconstructed ejection angle of the photoelectron, ϕ_k , associated with event k. Maps of the Stokes parameters I, Q, and U can then be obtained using (weighted) sums of $q_k = 2\cos 2\phi_k$ and $u_k = 2\sin 2\phi_k$, which can also include the correction for the energy- or event-dependent modulation factor μ_k :

$$I_{i,j} = W_{i,j}^{-1} \sum_{k} \frac{w_{k,i,j}}{\mu_{k}},$$

$$Q_{i,j} = W_{i,j}^{-1} \sum_{k} \frac{w_{k,i,j} q_{k,i,j}}{\mu_{k}},$$

$$U_{i,j} = W_{i,j}^{-1} \sum_{k} \frac{w_{k,i,j} u_{k,i,j}}{\mu_{k}},$$
(A1)

with $W_{i,j} \equiv \sum_k w_{k,i,j}$ the sum of the weights. This definition of Stokes I is chosen so that the polarization fraction can be expressed as $\Pi_{i,j} = \sqrt{Q_{i,j}^2 + U_{i,j}^2} / I_{i,j}$. Note that the division by μ_k ensures that the detector response to polarization, which is energy dependent, is taken into account.

The weights w_k can be based on the quality of the reconstruction of ϕ_k (Marshall 2021; Di Marco et al. 2022), or on the energy-dependent modulation factor (Vink & Zhou 2018), $w_k = \mu_k^{-2}$, or simply ignored, i.e., $w_k = 1$. The variances in the Stokes parameters are

$$\operatorname{Var}(I_{i,j}) = W_{i,j}^{-2} \sum_{k} \frac{w_{k,i,j}^{2}}{\mu_{k}^{2}},$$

$$\operatorname{Var}(Q_{i,j}) = W_{i,j}^{-2} \sum_{k} \frac{w_{k,i,j}^{2} q_{k,i,j}^{2}}{\mu_{k}^{2}},$$

$$\operatorname{Var}(U_{i,j}) = W_{i,j}^{-2} \sum_{k} \frac{w_{k,i,j}^{2} u_{k,i,j}^{2}}{\mu_{k}^{2}}.$$
(A2)

The polarization detection significance can be obtained by the methods described in, e.g., Kislat et al. (2015) and Vink & Zhou (2018), but we note here that in the absence of polarization the expectation values for the Stokes parameters are E[Q] = 0 and E[U] = 0, and that $\cos 2\phi$ and $\sin 2\phi$ are orthogonal functions. As a result the statistical quantity

$$S_{i,j} \equiv \frac{Q_{i,j}^2}{\text{Var}(Q_{i,j})} + \frac{U_{i,j}^2}{\text{Var}(U_{i,j})}$$
 (A3)

has a χ^2 distribution with two degrees of freedom. One can make a map of $S_{i,j}$, which we call a χ^2 map, that shows how consistent the observed polarization signal is with the null hypothesis (i.e., no polarization signal) in pixel (i, j). A large value of $S_{i,j}/\chi^2_{2,i,j}$ indicates, therefore, the presence of a polarization signal for pixel i, j with a confidence corresponding to χ^2_2 . A 3σ signal corresponds to $\chi^2_2 = 11.8$, 4σ to $\chi^2_2 = 19.3$, and 5σ to $\chi^2_2 = 28.7$.

 $\chi_2^2 = 19.3$, and 5σ to $\chi_2^2 = 28.7$. In the absence of an intrinsic polarization signal the expectation values for the variances are $E[\text{Var}(Q_{i,j})] = E[\text{Var}(U_{i,j})] = 2W_{i,j}^{-2} \sum_k (w_{k,i,j}^2 / \mu_k^2)$, since $E[(u^2 + q^2)] = 4$. Assuming that $\text{Var}(Q_{i,j}) \approx \text{Var}(U_{i,j})$, we can express the polarization degree as

$$\Pi_{i,j} = \sqrt{\frac{Q_{i,j}^2 + U_{i,j}^2}{I_{i,j}^2}} = \sqrt{\frac{S_{i,j} \text{Var}(Q_{i,j})}{I_{i,j}^2}}.$$
 (A4)

By noting that $S_{i,j}$ is χ_2^2 distributed and that the 99% confidence range corresponds to $\chi_2^2 = 9.21$ we see that the minimal detectable polarization (MPD₉₉) degree is

$$MDP_{99} = \sqrt{\frac{9.21 \times 2W_{i,j}^2 \sum_{k} (w_{k,i,j}^2 / \mu_k^2)}{W_{i,j}^{-2} \sum_{k} (w_{k,i,j}^2 / \mu_k)^2}}$$

$$= \frac{4.29}{\sqrt{\sum_{k} (w_{k,i,j}^2 / \mu_k)}}, \tag{A5}$$

equivalent to the expression derived by Kislat et al. (2015). The extraction of Stokes parameters over larger regions, after a local rotation of q_k and u_k , follows the same procedure as outlined here, except that the final outcome should not have a pixel index (i,j), but a region label.

Note that summing together $S_{i,j}$ over various pixels, by for example rebinning $(S_{i',j'} = \sum_{i,j} S_{i,j})$, results in yet another χ^2 distribution, but now with more degrees of freedom. For example, rebinning $S_{i,j}$ by 2×2 pixels, results in χ^2_8 distribution. Essentially this is an incoherent addition of the signal, so less sensitive than rebinning $Q_{i,j}$, $U_{i,j}$ (i.e., coherent summing), but it has the advantage that it is not sensitive to rotations of the polarization vector within the binned pixels region.

Appendix B Assessing the Nonthermal Contribution across Cas A

The radio emission from Cas A is almost exclusively caused by synchrotron radiation, but the emission in the 0.5–10 keV consists of a mixture of thermal radiation (line emission, bremsstrahlung, free–bound, and two-photon emission) and synchrotron radiation.

At the resolution of the Chandra X-ray observatory, the synchrotron emission stands morphologically apart (Hughes et al. 2000; Vink & Laming 2003; Hwang et al. 2004), being confined to narrow filaments, which may nevertheless also determine the

continuum in projection toward the rest of the SNR. The thermal emission from Cas A is dominated by emission from shocked ejecta (Laming & Hwang 2003). In order to prepare for the IXPE observations of Cas A, but also to estimate the contribution of the synchrotron radiation to each IXPE pixel as a function of energy, we modeled the emission from Cas A based on fitting Chandra X-ray spectra from the whole of Cas A, divided in tiles of 20" by 20". We used for the modeling the *xspec* package version 12.12 (Arnaud 1996), and concentrated on a single, 164 ks Chandra observation (ObsID 4638; Hwang et al. 2004).

The best-fit models per individual tiles were then folded through the spatial and spectral response functions of IXPE using the <code>ixpeobsim</code> instrumental response functions. For IXPE simulations we imposed a polarization degree and orientation on the X-ray synchrotron component. Before the launch of IXPE we used these simulations to test and optimize the analysis tools used for the results presented in this paper, but at the final stage, after indeed obtaining detections, we also used the simulations to translate the measured polarization degree into a polarization degree for just the synchrotron component. The prelaunch simulations indicated that the 3–6 keV band provided a more sensitive band for detecting polarization than the 4–6 keV (nearly) line-free band, as the broader band considerably improves the statistics.

The model consists of three thermal, nonequilibrium ionization, components, each with their own electron temperature per region, for which we used the vnei model (Borkowski et al. 2001), a power-law component to fit the synchrotron contribution, and the Galactic absorption model, tbabs (Wilms et al. 2000, which was also used for the abundances). The power-law slope was constrained to be $\Gamma = 2.8-3.4$, i.e., within $\Delta\Gamma = 0.3$ of the average spectral index for the synchrotron component of $\Gamma = 3.1$ measured by Helder & Vink (2008). The three vnei components represented the metal-dominated ejecta, with the components representing oxygen-, silicon-, and ironrich plasma. The abundances of oxygen, silicon, and iron elements were set to 10,000 times the solar value in order to simulate almost pure metal plasmas, which also enhances the contributions of free-bound and two-photon continuum (Greco et al. 2020). The oxygen-rich plasma was also responsible for the neon- and magnesium-line emission, and the silicon-rich plasma for the intermediate mass elements, but with the abundances of these elements as free parameters. Additional free parameters were the temperatures, constrained to 0.4–4 keV (4.5 keV for Fe); ionization ages ($n_e t$, constrained between 2×10^9 and 8×10^{11} cm⁻³s); the Galactic absorption column $(N_{\rm H})$; the normalizations of the emission components; Doppler shifts for the silicon- and iron-rich components.

Maps with the best-fit parameters of these models are shown in Figure 6.⁵¹ We do not claim that these are the best possible models for the emission of Cas A, as they are based on an automated procedure, sometimes manually assisted for particularly bad fits. But the final models fit the Chandra spectra generally well. This can be judged from the example spectral fits in Figure 7, one of which includes the worst fit in terms of the C-statistic. Despite the poor statistic, the overall spectral features are captured by the model. In general we find that the centroid of the Fe-K line emission is not well fitted. This centroid is determined by the plasma temperature, ionization

⁵¹ An archive of the complete data and model files (xcm files) can be found on Zenodo: 10.5281/zenodo.6597504, which also includes all data products used for this paper.

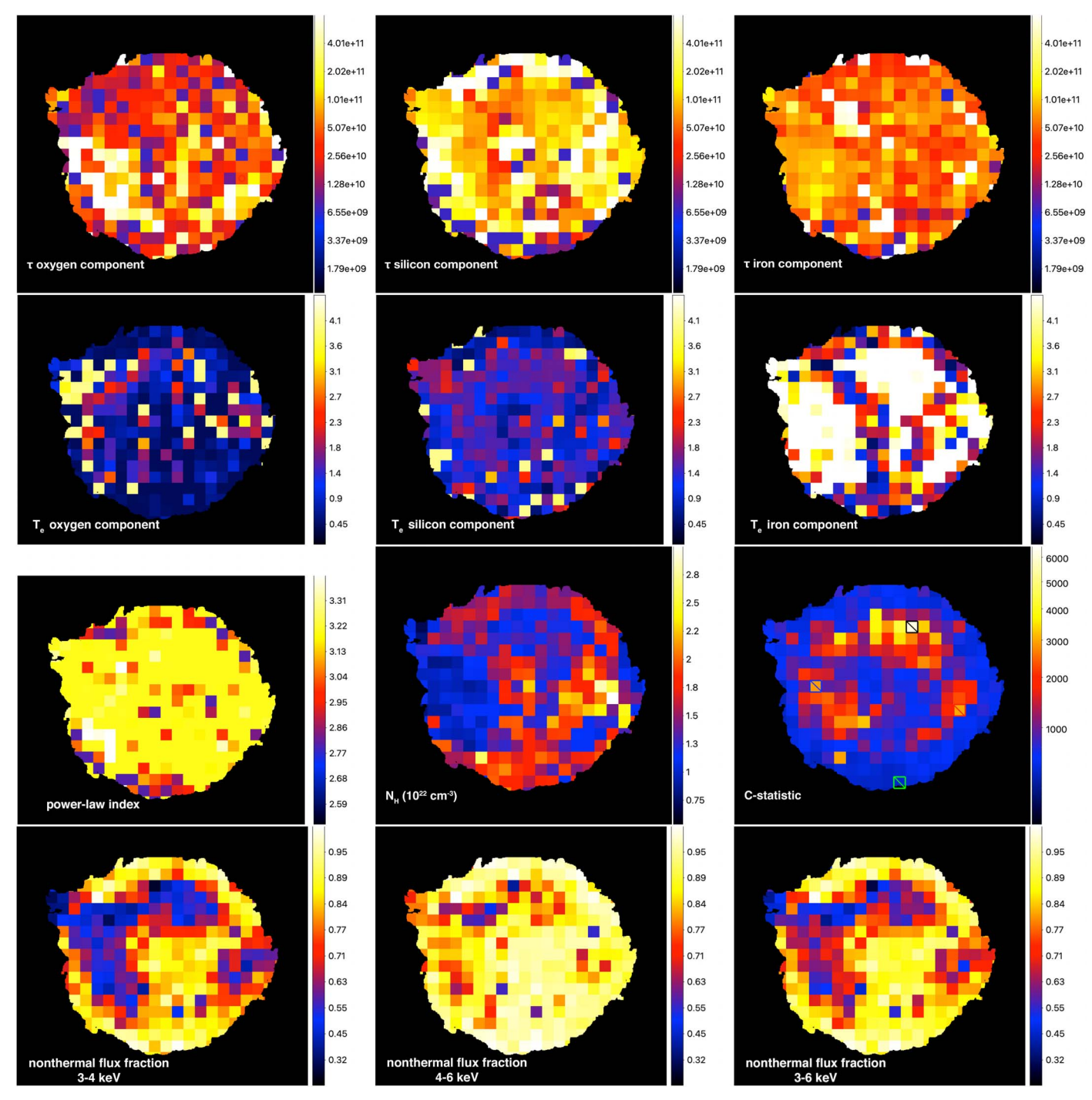


Figure 6. Examples of the maps of relevant parameters created from the output automated fitting of Chandra X-ray observations (ObsID 4638). We used these maps, and similar ones, to generate simulated IXPE event lists for assessing polarization degrees of the synchrotron components as a function of position and energy band. The top row shows the $\tau = n_{\rm e}t$ values in units of cm⁻³s for the oxygen-rich, silicon-rich (i.e., rich in intermediate mass elements), and iron-rich plasma components, respectively. The second row shows the absorption map ($N_{\rm H}$ in cm⁻²), the C-statistic values of the best fits, and the fraction of synchrotron radiation with respect to the overall flux in the 3–4 keV, 4–6 keV, and the combined 3–6 keV bands.

age, and Doppler shift. However, the ionization age and temperature also determine the iron L-shell emission between 0.8 and 1.4 keV, and cannot be arbitrarily varied. So a likely cause of the centroid mismatch is that the Fe-L and Fe-K emission may arise from various plasma components, suggesting that one plasma component for Fe-rich ejecta is not sufficient. The maps show also that the electron temperature of some components tend to get stuck at the predefined upper boundaries, at which point the fitting algorithm has difficulties

further optimizing the fitting results. This in particular is true for the electron temperature of the Fe-rich component, for which $T_{\rm e}=4.5~{\rm keV}$ for large parts of the SNR. The best-fit values for the power-law index are in most cases $\Gamma=3.2$, which is the starting value. This most likely reflects the insensitivity of the fit to the power-law index under the constrained condition that Γ lies within the range 2.8–3.4. The Galactic absorption map and the ionization age of the Si-rich component compare well with the ones provided in Hwang &

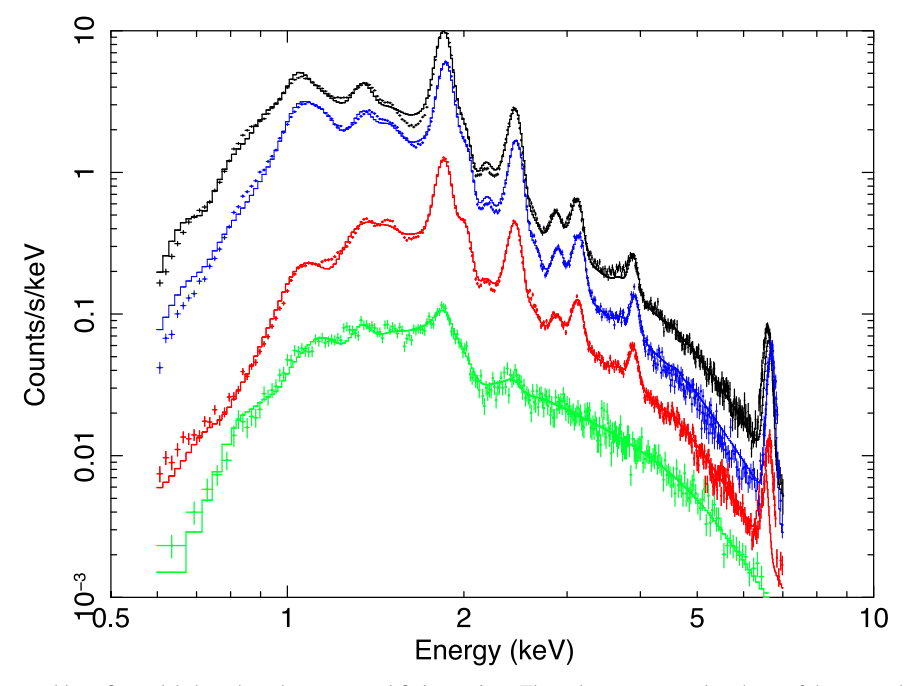


Figure 7. Four example spectra and best-fit models based on the automated fitting scripts. The colors correspond to those of the crossed squares in the C-statistic map in Figure 6. The black line corresponds to the worst C-statistic. The fits are generally satisfactory, but the iron line centroids appear off in the top three spectra.

Laming (2012). However, we note that Hwang & Laming (2012) did not include a full fitting of the nonthermal component in their analysis.

The values from the synchrotron continuum fraction were used to correct the observed polarization degree to the corresponding value for the synchrotron component. A perhaps surprising byproduct of the Chandra spectral mapping is that we find the fits indicate that the contribution of the synchrotron radiation to the overall continuum emission is surprisingly high, ranging from 38% to nearly 100%. Helder & Vink (2008) already showed that this might be the case based on the extrapolation of the hard X-ray continuum measured by BeppoSAX-PDS to the 4-6 keV band (their Figure 5), but estimated a more conservative 54% overall contribution. Nevertheless, the map of the synchrotron continuum fraction in Figure 6 matches well morphologically with Figure 6 (right) in Helder & Vink (2008) and the NuSTAR 10-15 keV map in Figure 6 (right) in Grefenstette et al. (2015). For completeness we show in the bottom panels of Figure 6 the nonthermal flux fraction in the 3-4 keV band (a mixture of line and continuum radiation), the 4-6 keV band (dominated by continuum radiation), and the combined band 3-6 keV band. The latter is the band chosen for the IXPE polarization measurements, based on prelaunch simulations. Although the 3%-4% keV band contains Ar-K and Ca-K line contributions, as can be seen in Figure 7, even in this band the nonthermal continuum fraction is large (>90%) in the X-ray synchrotron dominated regions, and still 25%–50% in the bright shell.

With ixpeobsim we simulated IXPE event lists for Cas A based on the grid of models for the Chandra spectra. These IXPE simulations showed that the 3–6 keV band is a good compromise between having a broad enough X-ray band to optimize statistics, and not too much degradation of the polarization signal due to the presence of Ar-K and Ca-K lines, but avoiding the very bright Si-K and S-K lines. Some Si-K and S-K line emission may be leaking into the 3–6 keV band

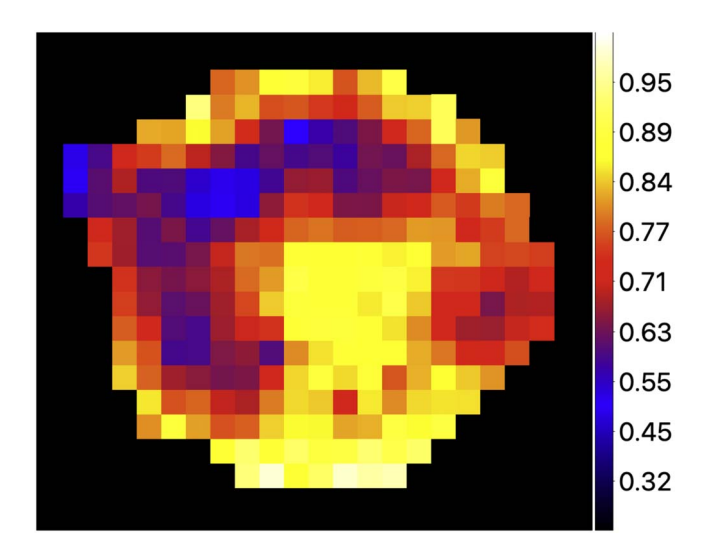


Figure 8. The nonthermal flux fraction in the 3–6 keV band inferred for IXPE, based on data simulated with ixpeobsim. The simulation used the Chandra spectral models as input parameters, using a full spectral and spatial response modeling—see the last panel of Figure 6.

due to the low spectral resolution of IXPE. The nonthermal flux fraction in the 3–6 keV inferred for IXPE is displayed in Figure 8, which includes all instrumental effects.

Appendix C Polarization Signal as a Function of Chosen Energy Band

The main text concentrates on the IXPE polarization signal analysis in the 3–6 keV band. In Table 2 we show for all regions combined and the FS+ RSW region the breakdown in polarization signal for the 3–4 keV and 4–6 keV band, as well as the inferred correction factor needed to obtain the polarization signal of the synchrotron component only, as based on the models in Appendix B. All values refer to

 Table 2

 Polarization Signal as a Function of Selected Energy Band

Band (keV)	MPD99 (%)	syn. corr.ª	Pol. Degree (%)	Angle (°)	Significance					
All regions combined										
3-4	1.1	1.5	1.2 ± 0.4	85.1 ± 8.8	2.6σ					
4–6	1.8	1.2	2.9 ± 0.6	86.1 ± 6.1	4.1σ					
3-6	1.0	1.4	1.8 ± 0.3	85.7 ± 5.3	4.9σ					
			FS+RWS							
3-4	1.9	1.4	1.8 ± 0.6	78.0 ± 10.3	2.2σ					
4–6	3.0	1.2	5.0 ± 1.0	92.1 ± 5.6	4.6σ					
3–6	1.7	1.3	3.0 ± 0.6	87.2 ± 5.4	4.8σ					

Note.

measurements based on the Stokes Q' and U' parameters, for which the definition of the polarization angle changes as a function of pixel position, assuming a circular symmetry with respect to the center of the SNR—see Section 2.2 for details.

Note that for the continuum-dominated, $4-6\,\mathrm{keV}$ band the polarization detection significance is 4.1σ for all regions combined and 4.6σ for the FS+RWS region. Although at a lower significance, the measurements in the continuum-dominated band supports the overall low polarization degree reported in the main text.

ORCID iDs

```
Jacco Vink https://orcid.org/0000-0002-4708-4219
Riccardo Ferrazzoli https://orcid.org/0000-0003-1074-8605
Patrick Slane  https://orcid.org/0000-0002-6986-6756
Ping Zhou https://orcid.org/0000-0002-5683-822X
Luca Baldini https://orcid.org/0000-0002-9785-7726
Enrico Costa https://orcid.org/0000-0003-4925-8523
Alessandro Di Marco https://orcid.org/0000-0003-0331-3259
Jeremy Heyl https://orcid.org/0000-0001-9739-367X
Frédéric Marin https://orcid.org/0000-0003-4952-0835
Tsunefumi Mizuno https://orcid.org/0000-0001-7263-0296
Melissa Pesce-Rollins https://orcid.org/0000-0003-1790-8018
John Rankin https://orcid.org/0000-0002-9774-0560
Carmelo Sgró https://orcid.org/0000-0001-5676-6214
Paolo Soffitta https://orcid.org/0000-0002-7781-4104
Martin C. Weisskopf  https://orcid.org/0000-0002-5270-4240
Ronaldo Bellazzini https://orcid.org/0000-0002-2469-7063
Raffaella Bonino https://orcid.org/0000-0002-4264-1215
Elisabetta Cavazzuti https://orcid.org/0000-0001-7150-9638
Niccoló Di Lalla https://orcid.org/0000-0002-7574-1298
Luca Latronico https://orcid.org/0000-0002-0984-1856
Simone Maldera https://orcid.org/0000-0002-0698-4421
Alberto Manfreda https://orcid.org/0000-0002-0998-4953
Francesco Massaro https://orcid.org/0000-0002-1704-9850
Nicola Omodei https://orcid.org/0000-0002-5448-7577
Ivan Agudo https://orcid.org/0000-0002-3777-6182
Matteo Bachetti https://orcid.org/0000-0002-4576-9337
Stefano Bianchi  https://orcid.org/0000-0002-4622-4240
Fiamma Capitanio https://orcid.org/0000-0002-6384-3027
Simone Castellano https://orcid.org/0000-0003-1111-4292
Stefano Ciprini https://orcid.org/0000-0002-0712-2479
Ettore Del Monte https://orcid.org/0000-0002-3013-6334
Victor Doroshenko https://orcid.org/0000-0001-8162-1105
Michal Dovčiak https://orcid.org/0000-0003-0079-1239
```

Steven R. Ehlert https://orcid.org/0000-0003-4420-2838 Teruaki Enoto https://orcid.org/0000-0003-1244-3100 Sergio Fabiani https://orcid.org/0000-0003-1533-0283 Javier A. Garcia https://orcid.org/0000-0003-3828-2448 Wataru Iwakiri https://orcid.org/0000-0002-0207-9010 Svetlana G. Jorstad https://orcid.org/0000-0001-6158-1708 Vladimir Karas https://orcid.org/0000-0002-5760-0459 Henric Krawczynski https://orcid.org/0000-0002-1084-6507 Fabio La Monaca https://orcid.org/0000-0001-8916-4156 Andrea Marinucci https://orcid.org/0000-0002-2055-4946 Alan P. Marscher https://orcid.org/0000-0001-7396-3332 Herman L. Marshall https://orcid.org/0000-0002-6492-1293 Giorgio Matt https://orcid.org/0000-0002-2152-0916 Fabio Muleri https://orcid.org/0000-0003-3331-3794 Alessandro Papitto https://orcid.org/0000-0001-6289-7413 George G. Pavlov https://orcid.org/0000-0002-7481-5259 Abel L. Peirson https://orcid.org/0000-0001-6292-1911 Maura Pilia https://orcid.org/0000-0001-7397-8091 Andrea Possenti https://orcid.org/0000-0001-5902-3731 Juri Poutanen https://orcid.org/0000-0002-0983-0049 Simonetta Puccetti https://orcid.org/0000-0002-2734-7835 Roger W. Romani https://orcid.org/0000-0001-6711-3286 Fabrizio Tavecchio https://orcid.org/0000-0003-0256-0995 Sergey Tsygankov https://orcid.org/0000-0002-9679-0793 Roberto Turolla https://orcid.org/0000-0003-3977-8760

References

```
Ahnen, M. L., Ansoldi, S., Antonelli, L. A., et al. 2017, MNRAS, 472, 2956
Anderson, M. C., Keohane, J. W., & Rudnick, L. 1995, ApJ, 441, 300
Arnaud, K. A. 1996, in ASP Conf. Ser. 101, XSPEC: The First Ten Years, ed.
   G. H. Jacoby & J. Barnes (San Francisco, CA: ASP), 17
Baldini, L., Barbanera, M., Bellazzini, R., et al. 2021, APh, 133, 102628
Baldini, L., Bucciantini, N., Di Lalla, N., et al. 2022, SoftX, 19, 101194
Ballet, J. 2006, AdSpR, 37, 1902
Bamba, A., Yamazaki, R., Yoshida, T., Terasawa, T., & Koyama, K. 2005,
   ApJ, 621, 793
Bell, A. R. 2004, MNRAS, 353, 550
Bellazzini, R., Angelini, F., Baldini, L., et al. 2003, Proc. SPIE, 4843, 383
Borkowski, K. J., Lyerly, W. J., & Reynolds, S. P. 2001, ApJ, 548, 820
Braun, R., Gull, S. F., & Perley, R. A. 1987, Natur, 327, 395
Bykov, A. M., Uvarov, Y. A., Bloemen, J. B. G. M., den Herder, J. W., &
   Kaastra, J. S. 2009, MNRAS, 399, 1119
Bykov, A. M., Uvarov, Y. A., Slane, P., & Ellison, D. C. 2020, ApJ, 899, 142
Costa, E., Soffitta, P., Bellazzini, R., et al. 2001, Natur, 411, 662
Di Marco, A., Costa, E., Muleri, F., et al. 2022, AJ, 163, 170
Dickel, J. R., & Jones, E. M. 1990, in IAU Symp. 140, Galactic and
   Intergalactic Magnetic Fields, ed. R. Beck, P. P. Kronberg, &
   R. Wielebinski (Dordrecht: Kluwer), 81
Dickel, J. R., & Milne, D. K. 1976, AuJPh, 29, 435
Dubner, G., & Giacani, E. 2015, A&ARv, 23, 3
Ferrazzoli, R., Muleri, F., Lefevre, C., Morbidini, A., & Amici, F. O. 2020,
   JATIS, 6, 048002
Flett, A. M., & Henderson, C. 1979, MNRAS, 189, 867
Funk, S. 2017, High-Energy Gamma Rays from Supernova Remnants, in
   Handbook of Supernovae, ed. A. Alsabti & P. Murdin, 1 (Cham:
   Springer), 1737
Gedalin, M., & Ganushkina, N. 2022, JPIPh, 88, 905880301
Ginzburg, V. L., & Syrovatskii, S. I. 1965, ARA&A, 3, 297
Ginzburg, V. L., & Syrovatskij, S. I. 1967, in IAU Symp. 31, Radio Astronomy
   and the Galactic System, ed. H. van Woerden, 411
Gotthelf, E. V., Koralesky, B., Rudnick, L., et al. 2001, ApJL, 552, L39
Greco, E., Vink, J., Miceli, M., et al. 2020, A&A, 638, A101
Grefenstette, B. W., Reynolds, S. P., Harrison, F. A., et al. 2015, ApJ, 802, 15
                       S, 161, 47
Gull, S. F. 1973, MN
Helder, E. A., & Vink, J. 2008, ApJ, 686, 1094
Helder, E. A., Vink, J., Bykov, A. M., et al. 2012, SSRv, 173, 369
Hu, Y., Xu, S., Stone, J. M., & Lazarian, A. 2022, arXiv:2207.06941
Hughes, J. P., Rakowski, C. E., Burrows, D. N., & Slane, P. O. 2000, ApJL,
   528, L109
```

^a Synchrotron correction fraction, i.e., the ratio of the inferred total flux over the nonthermal flux as based on the Chandra model fits.

```
Hwang, U., & Laming, J. M. 2012, ApJ, 746, 130
Hwang, U., Laming, J. M., Badenes, C., et al. 2004, ApJL, 615, L117
Inoue, T., Shimoda, J., Ohira, Y., & Yamazaki, R. 2013, ApJL, 772, L20
Jones, T. J., Rudnick, L., DeLaney, T., & Bowden, J. 2003, ApJ, 587, 227
Jun, B.-I., & Norman, M. L. 1996, ApJ, 472, 245
Kenney, J. D., & Dent, W. A. 1985, ApJ, 298, 644
Kislat, F., Clark, B., Beilicke, M., & Krawczynski, H. 2015, APh, 68, 45
Koyama, K., Petri, R., Gotthelf, E. V., et al. 1995, Natur, 378, 255
Laming, J. M., & Hwang, U. 2003, ApJ, 597, 347
Malkov, M. A., & Drury, L. 2001, RPPh, 64, 429
Marcowith, A., Bret, A., Bykov, A., et al. 2016, RPPh, 79, 046901
Marshall, H. L. 2021, AJ, 162, 134
Mayer, C. H., & Hollinger, J. P. 1968, ApJ, 151, 53
Patnaude, D. J., & Fesen, R. A. 2009, ApJ, 697, 535
Peirson, A. L., & Romani, R. W. 2021, ApJ, 920, 40
Pohl, M., Yan, H., & Lazarian, A. 2005, ApJL, 626, L101
Rankin, J., Muleri, F., Tennant, A. F., et al. 2022, AJ, 163, 39
Reed, J. E., Hester, J. J., Fabian, A. C., & Winkler, P. F. 1995, ApJ, 440, 706
Rosenberg, I. 1970, MNRAS, 151, 109
```

```
Rothenflug, R., Ballet, J., Dubner, G., et al. 2004, A&A, 425, 121
Sato, T., Katsuda, S., Morii, M., et al. 2018, ApJ, 853, 46
Shklovsky, J. S. 1954, Liege International Astrophysical Colloquia, Vol. 5
  (Liege: Louvain), 515
Soffitta, P., Baldini, L., Bellazzini, R., et al. 2021, AJ, 162, 208
Sun, X. H., Reich, P., Reich, W., et al. 2011, A&A, 536, A83
Thorstensen, J. R., Fesen, R. A., & van den Bergh, S. 2001, AJ, 122, 297
Uchiyama, Y., & Aharonian, F. A. 2008, ApJL, 677, L105
Vink, J., & Laming, J. M. 2003, ApJ, 584, 758
Vink, J., Patnaude, D. J., & Castro, D. 2022, ApJ, 929, 57
Vink, J., & Zhou, P. 2018, Galax, 6, 46
Völk, H. J., Berezhko, E. G., & Ksenofontov, L. T. 2005, A&A, 433,
Weisskopf, M., Soffitta, P., Baldini, L., et al. 2022, JATIS, 8, 026002
West, J. L., Jaffe, T., Ferrand, G., Safi-Harb, S., & Gaensler, B. M. 2017,
   ApJL, 849, L22
Wilms, J., Allen, A., & McCray, R. 2000, ApJ, 542, 914
Xie, F., Ferrazzoli, R., Soffitta, P., et al. 2021, APh, 128, 102566
Zirakashvili, V. N., & Ptuskin, V. S. 2008, ApJ, 678, 939
```